Experimental and Numerical Investigation on the Transient Cavitating Flows in a Mixed Flow Pump With Different Number of Blades at Startup

Zhang Desheng[1]
Mem. ASME
Research Center of Fluid Machinery Engineering and Technology,
Jiangsu University,
Zhenjiang 212013, China
e-mail: zds@ujs.edu.cn

Zhou Qiang
PowerChina Huadong Engineering Corporation Limited,
Hangzhou 310014, China
e-mail: Zhouqiang1420@126.com

Gu Qi
Shanghai Institute of Applied Mathematics and Mechanics,
School of Mechanics and Engineering Science,
Shanghai University,
Shanghai 200072, China
e-mail: 527224117@qq.com

Zhang Guangjian
Research Center of Fluid Machinery Engineering and Technology,
Jiangsu University,
Zhenjiang 212013, China
e-mail: eddyzhang_ujs@hotmail.com

Xu Bin
Research Center of Fluid Machinery Engineering and Technology,
Jiangsu University,
Zhenjiang 212013, China
e-mail: norkistar@ujs.edu.cn

Geng Linlin
Research Center of Fluid Machinery Engineering and Technology,
Jiangsu University,
Zhenjiang 212013, China
e-mail: mosu2010@outlook.com

B. P. M. (Bart) van Esch
Mem. ASME
Department of Mechanical Engineering,
Eindhoven University of Technology,
Eindhoven 5600MB, The Netherlands
e-mail: b.p.m.v.esch@tue.nl

Experimental and Numerical Investigation on the Transient Cavitating Flows in a Mixed Flow Pump With Different Number of Blades at Startup

The objective of this paper is to experimentally and numerically investigate the transient cavitation flow during the startup process of mixed flow pump with emphasis on studying the influence of blade numbers. The transient cavitation simulation was studied based on the improved SST k–ω *turbulence model and the Zwart cavitation model. Firstly, in order to obtain the relationship between transient flow rate and the variation of rotational speed at startup, a theoretical analysis based on the fast transients of centrifugal pump was first applied to mixed flow pump and was verified by the current experiment study. Subsequently, the influence of blade number on the cavitation flow in the startup was studied. It is found that the transient cavitation could be classified into four stages regardless of the number of blades: no cavitation stage, the cavitation growth stage, the cavitation reduction stage and the cavitation stabilization stage. However, the blade number does have an impact on the spatial-temporal evolution of cavitation. More specifically, when the blade number increases, the initial cavitation appeared lately, the coverage area of the triangular cavitation cloud and sheet cavitation both decreased, and the increase in blade number has a better inhibitory effect on the sheet cavitation at the cavitation growth stage, and can make sheet cavitation disappear more quickly at the cavitation reduction stage.* [DOI: 10.1115/1.4052863]

1 Introduction

Mixed-flow pump is widely used in ship propulsions and sealed hydraulic systems due to its advantages of large flow rate and high efficiency [1,2]. A typical application of mixed flow pump is to launch underwater weapon, which requires the pump to operate stably during the startup process. However, the startup process of pump can cause intensive pressure fluctuations and power impacts, and meanwhile it is always accompanied by the generation of the transient cavitation, which induces hydraulic vibrations and flow noise [3–6]. Hence, in order to improve the transient performance and enhance the cavitation resistance of the mixed-flow pump, it is important to investigate the transient cavitation at startup.

In the past decades, researchers mainly focused on the transient external characteristics of turbomachinery at the startup process using experimental and theoretical methods. Tsukamoto et al. [7–9] experimentally explored the transient external characteristics of a radial flow pump during a rapid startup. The experimental results show that there is a difference between dynamic and quasi-steady characteristics of the pump during its starting period. They inferred that the impulsive pressure and the lag in circulation formation around impeller vanes play predominant roles for the difference. Saito et al. [10] found that the mass of water in the pipeline, the valve opening percentage, and the starting time were responsible for the departure of the dynamic characteristics of a pump during startup from the normal steady-state performance.

[1]Corresponding author.

Contributed by the Fluids Engineering Division of ASME for publication in the Journal of Fluids Engineering. Manuscript received February 10, 2021; final manuscript received October 24, 2021; published online January 20, 2022. Assoc. Editor: Stefan aus der Wiesche.

Dazin et al. [11,12] proposed a theoretical expression of the instantaneous head by solving transient angular momentum and energy equation, including terms of angular acceleration, flow acceleration, and velocity profile variation. In addition, they found that the performance of a pump not only depends on the acceleration rate and flow rate but also on the instantaneous velocity profile variation at startup.

Besides the transient external characteristics, another concern is the cavitation, which is induced by the significant pressure fluctuations during the startup process. Tanaka et al. [13,14] extended the experimental studies on the dynamic characteristics of noncavitating centrifugal pumps to the cavitating case. The results indicated that the oscillating cavitation at startup and water column separation at the sudden stop of the pump caused the fluctuations of pressure and flow rate. Moreover, the occurrence of transient pressure and flow rate fluctuations were predicted by inspecting the critical condition of oscillating cavitation and water column separation [15]. Duppla et al. [16,17] analyzed the evolution of the local amount of vapor in blade channels of the pump by fast X-ray imaging experiment, and they found that the occurrence of local cavitation during its fast startup, induced a sudden drop in the internal pressure of the pump and caused a water hammer at the inlet and outlet. Wu et al. [18,19] experimentally studied the transient cavitation characteristics at startup, and they concluded that the accelerated process had a certain inhibitory effect on the generation of cavitation.

In addition, the leakage flow is inevitable due to the existence of the tip clearance in turbomachines like mixed flow pumps and axial flow pumps [20]. The leakage flow interacts with the main flow, rolling up into a tip leakage vortex (TLV), which is likely to induce cavitation [21]. The cavitating flow in the tip region is extremely complicated, thus the experimental techniques including particle image velocimetry and high-speed photography were applied to investigate this type of cavitating flow. Tan et al. [22] and Zhang et al. [23,24] used high-speed photography experiments and discovered that the cavitating structure in the axial flow pump is mainly composed of sheet cavitation on the blade surface, blowing cavitation, tip leakage vortex cavitation, and tip gap cavitation, and they clarified the formation mechanism of these different types of cavitation. Miorini et al. [25–27] conducted a large numbers of particle image velocimetry experiments on the structure of the leakage vortex. They revealed the forming process of the leakage vortex and the separation phenomenon in the shear layer. Zhao et al. [28] analyzed the flow field just upstream the leading edge (LE) at different cavitation conditions, and found that the cavitation evolution has an influence on the incidence angle, which further affects the flow structures on the suction surface (SS).

In recent years, computational fluid dynamic (CFD) has been widely used to study the transient flow during a pump rapid starting period. Wang et al. [29] adopted the dynamic mesh method in a 2D simulation of a centrifugal pump during its startup period. They analyzed the internal unsteady flow structure and its relationship with the external transient characteristics. Wu et al. [30] used the sliding mesh technique to numerically simulate the internal flow of a centrifugal pump during the quick startup process, and experiments were also carried out to verify the reliability of the simulation. Li et al. [31,32] simulated the transient flow evolution in a centrifugal pump during its rapid startup by using the numerical dynamic slip region method. They analyzed the relations between the instantaneous flow evolutions and the corresponding transient flow rate, head, efficiency and power. Moreover, Zhang [33] performed a three-dimensional CFD simulation to reveal the difference of transient behavior during the startup period when centrifugal pumps transport a single-phase water and a solid–liquid two-phase flow. At summarized above, most of the accelerated flow research focused on the pump characteristic curve. However, there are few numerical studies on the evolution of cavitation during the startup process due to the lack of solution methods in acquiring the transient flows in mixed flow pumps during transient operations.

The purpose of this paper is to reveal the evolution of cavitation and to explore the influence of blade numbers on transient cavitation during the mixed flow pump startup process. This study is organized as follows: the experimental methodology and setup are presented in Sec. 2; the numerical models and setups are illustrated in Sec. 3; the theoretical analysis is described in Sec. 4; in Sec. 5 the evolution of transient cavitation at startup are analyzed; in Sec. 6 the final conclusions are summarized.

2 Experimental Setup

2.1 Experimental Apparatus. The mixed flow pump model is installed in a closed test loop at the National Fluid Machinery Laboratory, Jiangsu University, as shown in Fig. 1(*a*). The major components of the test loop include a butterfly valve, a gate valve, a booster pump and a water tank. A cavitation tank is located above the water tank, and it is partially filled with water forming a free surface. A vacuum pump is connected with the cavitation tank from the top, and it is used to adjust the static pressure at the inlet of the pump for different cavitation numbers. In order to conduct high speed imaging experiments for the mixed flow pump model, the test section (i.e., the pump casing) is made of transparent Perspex. A turbine flowmeter is used to control the final flow conditions after the transients or to characterize stabilized flow conditions. Due to their acquisition frequency is too small to accurately catch the flow rate rise evolutions during a fast startup. Thus, a method (in Sec. 4) is provided to obtain the transient results of flow rate.

2.2 Experimental Procedures. The layout of high-speed imaging test is shown in Fig. 1(*b*). A high-speed camera was fixed on the side of the test section, and the recording frequency was 4000 Hz. First, the model pump ran at 1450 r/min for some time to remove the residual air in the pipe, and then stop the pump after adjusting the flow condition to the rated flow rate (126.62 L/s). Second, the rotational speed of the mixed flow pump was set to the startup mode under the control of the frequency inverter. The detailed settings are that the whole operation process of the mixed flow pump takes 10 s: during the first 2 s, the rotational speed of

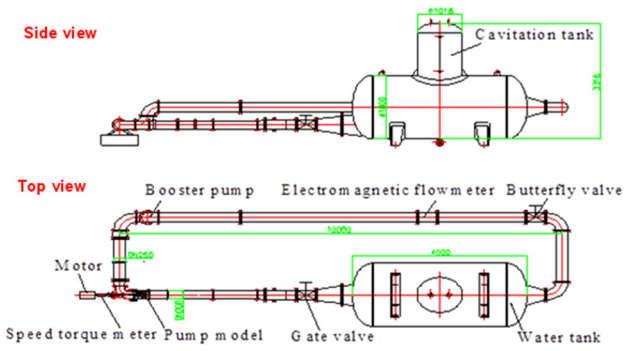

(*a*)

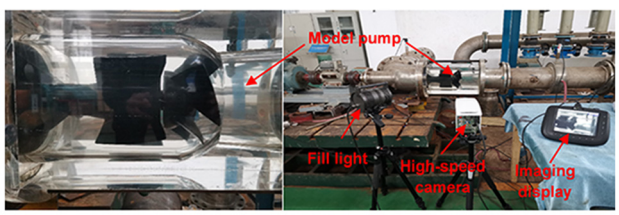

(*b*)

Fig. 1 Schematics of mixed flow pump test loop and high-speed imaging photography system (*a*) schematics diagram and overall dimensions of the mixed flow pump loop and (*b*) layout of high-speed imaging experiment)

the mixed flow pump accelerates from zero to 1450 r/min, and then the pump rotates at a constant speed (1450 r/min) for the next 8 s. Third, the vacuum pump was used to extract the air in the cavitation tank in order to reduce the pump inlet pressure. When the pump inlet pressure dropped to 50 kPa, stop the vacuum pump. Finally, once the inlet pressure was stable at 50 kPa, starting the mixed flow pump according to the setting procedure of the inverter. At the same time, the pressure at the inlet and outlet of the pump and the cavitation structure were recorded using the pressure sensor and high speed camera, respectively.

2.3 Measurement Uncertainty. The measurement uncertainty analysis was performed based on the ANSI/ASME PTC 19.1 [34,35]. The uncertainty of the unsteady pressure transducer is ±1%. The measurement uncertainty has been conducted in our previous work [36]. The measurement uncertainty was symbolized by the coverage factor of $k = 2$, which provides a confidence level about 95%. Figure 2 shows the repeatability validation of experimental results in the impeller with $Z_i = 3$. It is obtained by six sets of repeated tests across a range of conditions. The flow rate coefficient and head coefficient are defined as $\Phi = 2\pi Q/(\Omega D_2^3)$, $\Psi = (2\pi)^2 gH/(\Omega D_2)^2$ (Ω is the impeller angular velocity, rad/s; D_2 is the discharge pipe diameter, m), respectively. The results show that the maximum error occurs at $\Phi = 0.134(0.4Q_{opt})$, with the standard deviation of 0.0232, and the minimum error occurs at $\Phi = 0.335(1.0Q_{opt})$, with the standard deviation of 0.0167. The results prove the stability of the equipments and the repeatability of the results.

3 Numerical Simulation

3.1 Governing Equations. In the present investigation, the homogeneous mixture model was employed to simulate the vapor/liquid two-phase fluid, so the multiphase fluid components share the same velocity and pressure [37]. The continuity and momentum equations for the mixture flow are

$$\frac{\partial \rho_m}{\partial t} + \frac{\partial (\rho_m u_j)}{\partial x_j} = 0 \tag{1}$$

$$\frac{\partial (\rho_m u_i)}{\partial t} + \frac{\partial (\rho_m u_i u_j)}{\partial x_j} = -\frac{\partial p}{\partial x_i} + \frac{\partial p}{\partial x_j}\left[(\mu_m + \mu_t)\left(\frac{\partial u_i}{\partial x_j} + \frac{\partial u_j}{\partial x_i} - \frac{2}{3}\frac{\partial u_k}{\partial x_k}\delta_{ij}\right)\right] \tag{2}$$

where the mixture density ρ_m is defined as $\rho_m = \alpha_l \rho_l + \alpha_v \rho_v$, and ρ_l, ρ_v, α_l, α_v are the densities of the liquid and the vapor, the volume fractions of the liquid and the vapor, respectively; u is the velocity, p is the pressure, the mixture dynamic viscosity is defined as $\mu_m = \mu_l \alpha_l + \mu_v \alpha_v$, and μ_l, μ_v are, respectively, the liquid and vapor dynamic viscosity, μ_t is the turbulent viscosity.

3.2 Modified Turbulent Viscosity. Menter et al. [38] first developed the SST k–ω model, which is a combination of the k-ε model and the k–ω model. Bardina et al. [39] validated the SST k–ω model is suitable for predicting flow separation with adverse pressure gradients. The turbulent viscosity μ_t in the SST k–ω is shown as follows:

$$\mu_t = \frac{\rho_m k}{\omega} \frac{1}{\max\left(\frac{1}{a^*}, \frac{SF_2}{a_1 \omega}\right)} \tag{3}$$

where S is the strain rate; ω is the specific dissipation rate; k is the turbulent kinetic energy; F_2 is a function, which is 1.0 for boundary-layer flows and zero for free shear layers, $a_1 = 0.31$. a^* is a coefficient, which damps the turbulent eddy viscosity

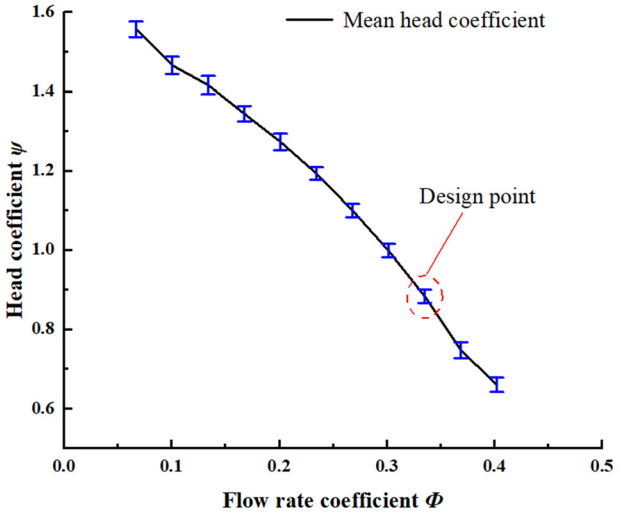

Fig. 2 The results of repeatability validation in the model pump with blade number $Z_i = 3$ (Different tests are repeated under the same conditions)

representing a low-Reynolds-number correction, $a^* = 1$ in a high-Reynolds-number flow.

However, many studies [40–46] have showed that the k–ε and the k–ω turbulence models overestimate the turbulent viscosity in the region of cavity closure. Thus, a mixture density correction $f(\rho_m)$ proposed by Reboud et al. [40] was used to modify the turbulent viscosity. This correction is as follows:

$$f(\rho_m) = \rho_v + \left(\frac{\rho_m - \rho_v}{\rho_l - \rho_v}\right)^n (\rho_l - \rho_v) \quad (n = \text{constant and } n \geq 1) \tag{4}$$

Taking into account this correction, the modified turbulent viscosity in SST k–ω turbulence model was defined as

$$\mu_{t-DCM} = \mu_t f(\rho_m) = \frac{k}{\omega} \frac{\left[\rho_v + \frac{(\rho_m - \rho_v)^n}{(\rho_l - \rho_v)^{n-1}}\right]}{\max\left(\frac{1}{a^*}, \frac{SF_2}{a_1 \omega}\right)} \quad (n = \text{constant and } n \geq 1) \tag{5}$$

This density corrected method has been demonstrated by a lot of numerical studies [41–45] on simulating the cavitating flow around the hydrofoils, and the exponent value is recommended to be 10 [46,47], which is also used in the present simulations.

The evidence on the correct implementation by hydrofoil cloud shedding has been provided in our previous work [24], as shown in Fig. 3. The entire dynamic process of the sheet cavity inception, growth, shedding, and collapse was observed successfully, which agrees well with the experimental results. Moreover, the modified eddy-viscosity was successfully applied to simulate the unsteady TLV cavitation patterns and unstable suction-side-perpendicular cavitating vortice collapse of the axial flow pump in the Ref. [24]. The way implemented is that the code of the modified turbulent eddy viscosity was written by Cfx experssion language (CEL) language and embedded into CFD software ANSYS-CFX.

3.3 Cavitation Model. For cavitation modeling, this study adopted the Zwart cavitation model [37], which is derived from the Rayleigh–Plesset equation. The governing equation of vapor volume fraction is given as

$$\frac{\partial (\alpha_v \rho_v)}{\partial t} + \frac{\partial (\alpha_v \rho_v u_j)}{\partial x_j} = \dot{m}^+ + \dot{m}^- \tag{6}$$

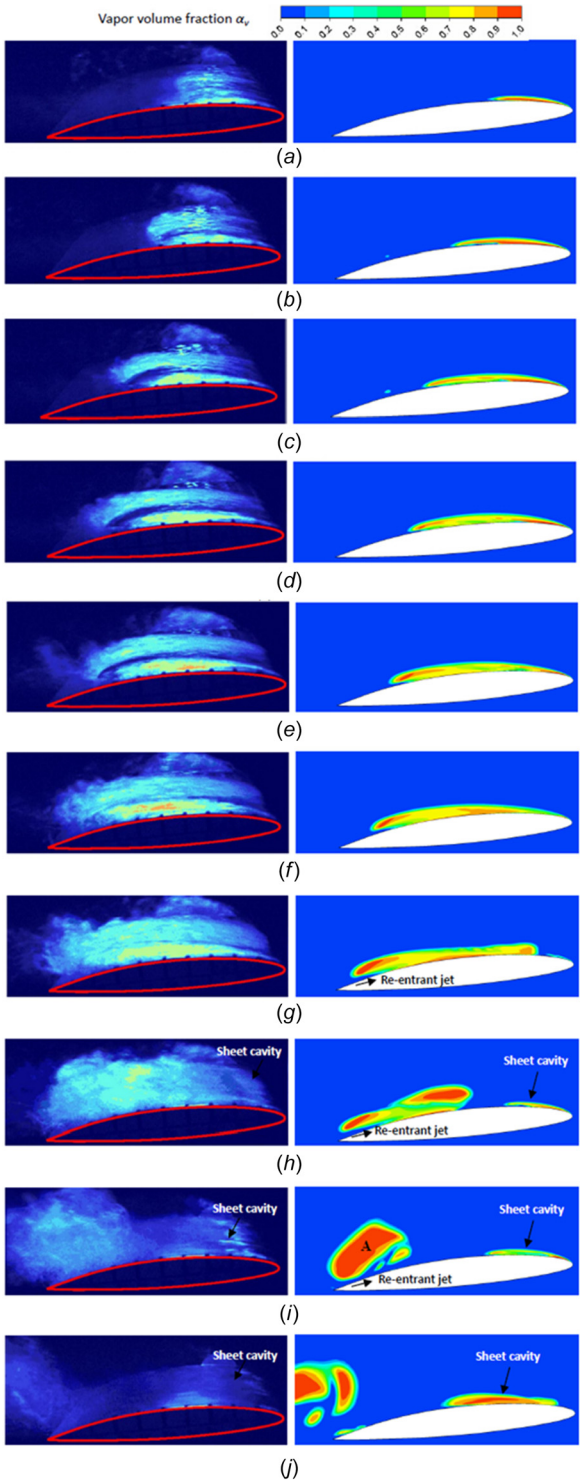

Fig. 3 Comparison of experimental and numerical cloud cavitation shedding flows [24]. Left: 3D experimental visualizations; right: 2D numerical instantaneous vapor fraction α_v.

where the evaporation rate $\dot{m}^+$ and the condensation rate $\dot{m}^-$ are defined as follows:

$$\dot{m}^+ = C_e \frac{3\alpha_{nuc}(1-\alpha_v)\rho_v}{R_b}\sqrt{\frac{2}{3}\frac{p_v - p}{\rho_l}} \quad (p \le p_v) \tag{7}$$

$$\dot{m}^- = C_c \frac{3\alpha_v \rho_v}{R_b}\sqrt{\frac{2}{3}\frac{p - p_v}{\rho_l}} \quad (p \ge p_v) \tag{8}$$

where R_b is the bubble radius; α_{nuc} is the nucleation site volume fraction; C_e and C_c are empirical coefficients for the evaporation and condensation processes, respectively. The default constants for Zwart cavitation model are listed as $R_b = 1 \times 10^{-6}$ m, $\alpha_{nuc} = 5 \times 10^{-4}$, $C_e = 50$, and $C_c = 0.01$.

3.4 Pump Model, Meshing and Boundary Conditions

3.4.1 Pump Model. Figure 4(*b*) shows the schematic diagram of the mixed flow pump with the specific speed n_s of 829 in this work and the detailed parameters are listed in Table 1. The design flow rate is 126.62 L/s; the design number of the impeller is 3; and the tip clearance is 0.25 mm. Besides, as shown in Fig. 4(*a*), three impellers with different blade numbers are considered to study the influence on transient cavitation at startup. The inlet pipe is extended to $4D_1$ for a better numerical convergence, and the whole computational zone is shown in Fig. 4(*c*).

3.4.2 Meshing Technique and Independence Verification. All the fluid domains are discretized with hexahedron structured grids, which were beneficial to a smaller truncation error and a better convergence, as shown in Fig. 5(*a*). The grids around the impeller

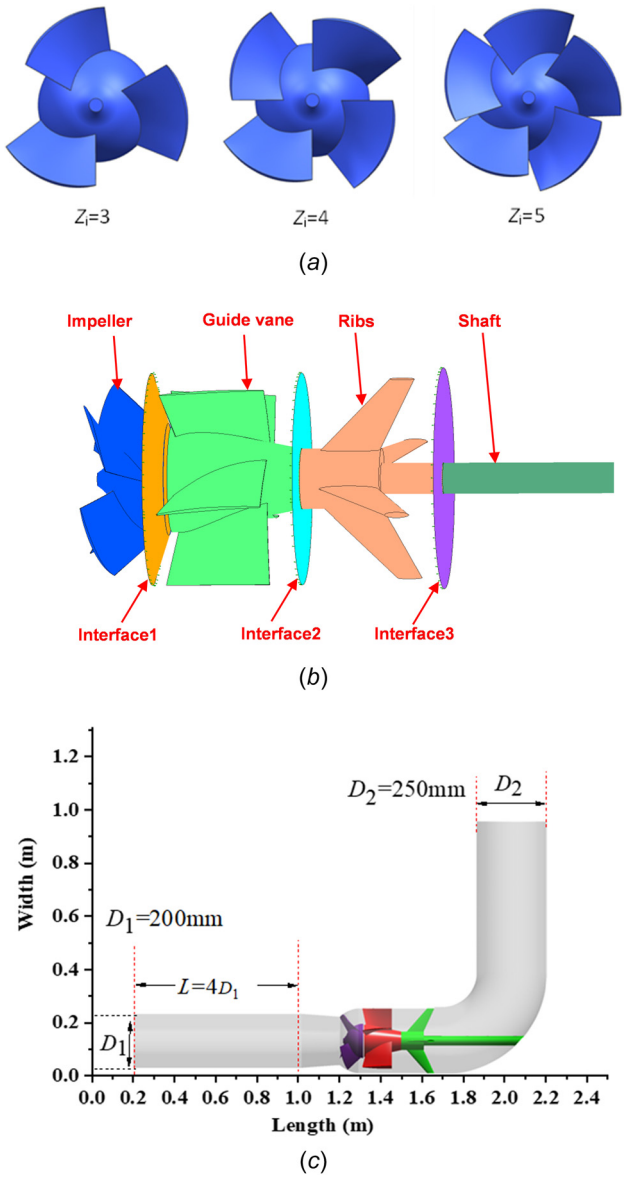

Fig. 4 Pump model: (*a*) impeller, (*b*) pump geometry, and (*c*) computational zone

Table 1 Main parameters of the pump model

Parameter	Value
Rated flow rate Q(L/s)	126.62
Rated head H(m)	2.99
Design impeller blades Z_i	3
Number of stay vane blades Z_s	5
Design rotational speed n(r/min)	1450
Impeller inlet diameter D_0(mm)	180
Inlet pipe diameter D_1(mm)	200
Discharge pipe diameter D_2(mm)	250
Tip clearance h(mm)	0.25

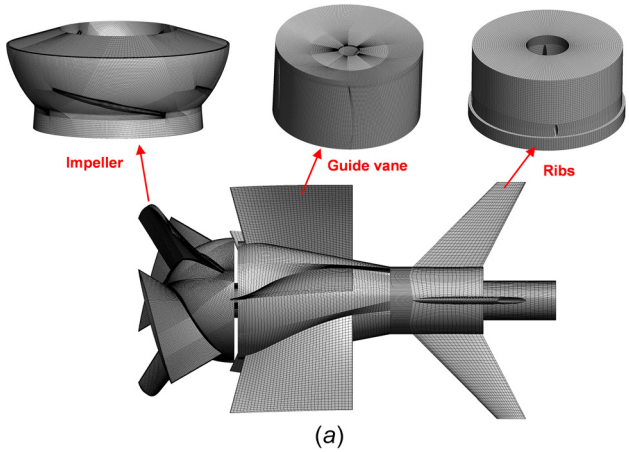

(a)

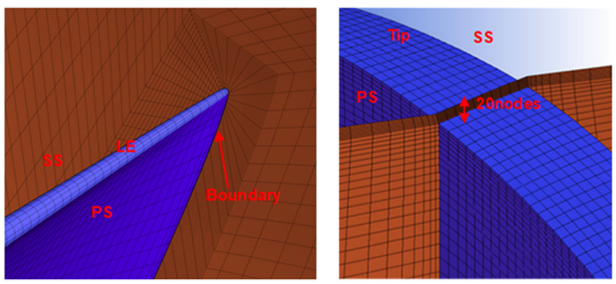

(b) (c)

Fig. 5 Mesh arrangement: (*a*) surface mesh of main components, (*b*) mesh near the blade surface, and (*c*) refined mesh near tip

blades and the guide vane blades were refined with the O-topology method. A boundary layer mesh shown in Fig. 5(*b*) was created. The automatic near-wall treatment for the omega-based model was used [38], which can switch automatically from a typical wall function approach to a low-Re number model by blending

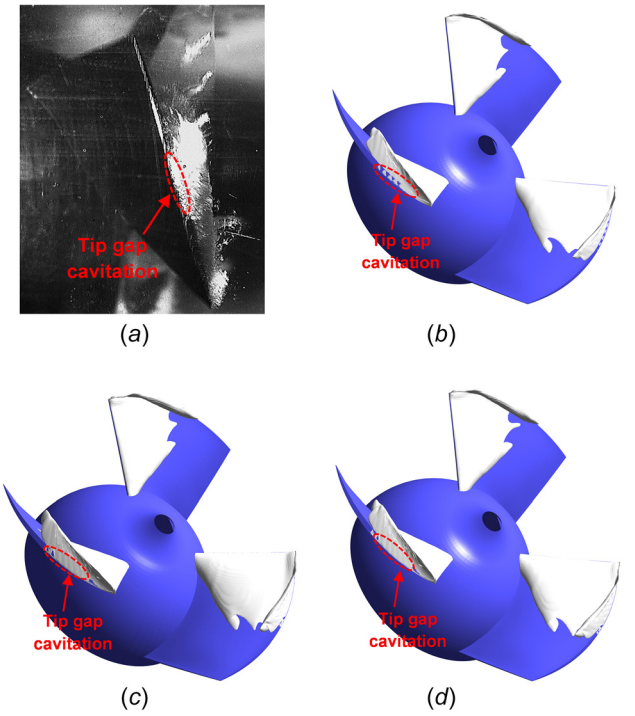

(a) (b) (c) (d)

Fig. 6 Comparison of experimental and numerical tip gap cavitation in the gap with different nodes ($Z_i = 3$, $t = 1.8$ s, $\alpha_v = 0.1$): (*a*) experimental results, (*b*) 15 nodes in the gap, (*c*) 20 nodes in the gap, and (*d*) 25 nodes in the gap

the wall value for ω between the logarithmic and the near wall formulation as the mesh is refined. The mesh has to be refined in the tip region to better capture the tip leakage flow. Therefore, the independence test of mesh density is conducted to examine the reliability and accuracy of the mesh arrangement. As shown in Table 2, three sets of meshes in impeller are selected to study. In the present research, the impeller with $Z_i = 3$ is selected to analyze. Figure 6 is the experimental and numerical results of tip gap cavitation in the impeller with $Z_i = 3$. The area of the tip gap cavitation in Fig. 6(*b*) is lower than that in experimental results (Fig. 6(*a*)). The locations and area of the tip gap cavitation in Figs. 6(*c*) and 6(*d*) show a quite good agreement with the experimental results (Fig. 6(*a*)). It is proved that the arrangement of 20 nodes and 25 nodes can accurately capture the flow characteristics around the tip clearance region. According to the results shown in Table 2 and considering the computing time and resources, 20 nodes were setup in the tip gap, as shown in Fig. 5(*c*). The value of $y+$ on the blade surface is varied from 1 to 50, and the average value of $y+$ on the surface is about 28.5, as shown in Fig. 7. Finally, the mesh arrangements of 10.16×10^6, 10.77×10^6, and 13.91×10^6 nodes was finally used for the impeller with $Z_i = 3$, $Z_i = 4$, and $Z_i = 5$, respectively.

Table 2 Results of grid independence study

Blade numbers	Mesh nodes (million)	Nodes in the gap	Head (m)	Efficiency (%)	Mean y^+
$Z_i = 3$	8.09	15	2.81	75.12	96.53
	10.16	20	2.97	76.37	28.5
	11.14	25	2.98	76.39	28.23
$Z_i = 4$	9.94	15	3.15	75.23	67.60
	10.77	20	3.19	75.56	27.12
	11.21	25	3.18	75.61	26.93
$Z_i = 5$	8.37	15	3.44	73.31	102.1
	11.67	20	3.47	74.11	23.15
	13.91	25	3.49	75.13	22.17

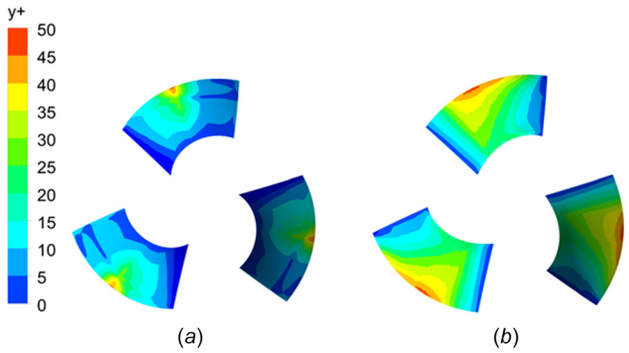

Fig. 7 Distribution of $y+$ on the surface of blades ($Z_i = 3$): (*a*) pressure surface and (*b*) suction surface

Table 3 Main settings in numerical simulation

Item	Setting
Inlet boundary condition	Total pressure(50 kPa)
Outlet boundary condition	Q
rotational speed	N
Startup time t_s	2 s
Total time T_{total}	4 s
RMS residuals	10^{-5}
Time step	4×10^{-4} s
Advection scheme	High resolution

Table 4 The coefficients of Eq. (10)

a_1	75.02	a_2	34.1	a_3	−1003	a_4	1048	a_5	44.34	a_6	32..28
b_1	18.86	b_2	3.18	b_3	6.17	b_4	6.15	b_5	9.98	b_6	2.15
c_1	8.51	c_2	1.27	c_3	2.31	c_4	2.34	c_5	4.72	c_6	0.85

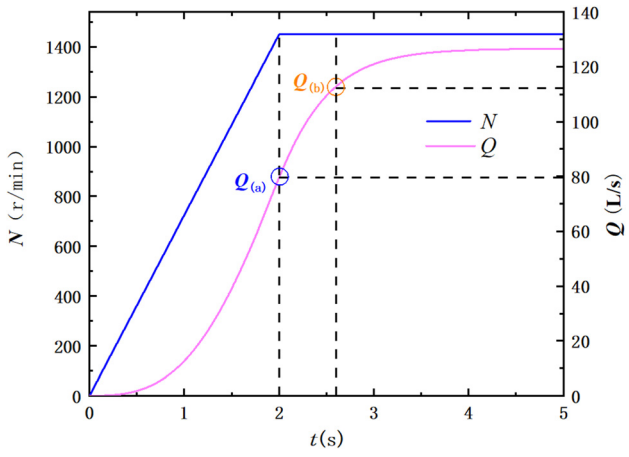

Fig. 8 The boundary conditions setting of speed and flow rate Q in numerical simulation (startup time $t_s = 2$ s)

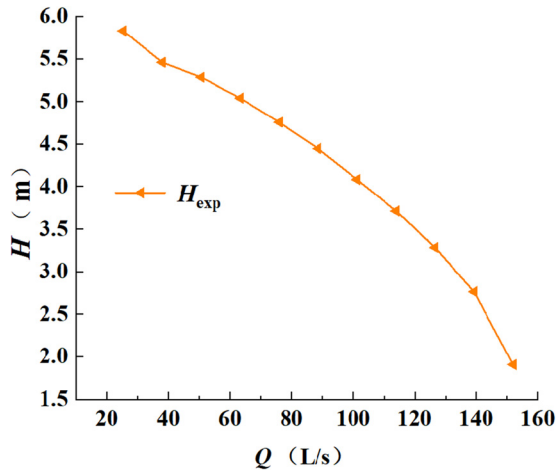

Fig. 9 Pump performance for the impeller with $Z_i = 3$ obtained by experiment (pump is running in a steady-state with a speed of 1450 r/min)

3.4.3 Boundary Conditions. The numerical calculations were conducted in ANSYS-CFX. The boundary conditions are specified according to the experimental configuration, and the main numerical settings applied in the transient calculations are presented in Table 3. A second order implicit time stepping is adopted for the time discretization. And the time-step is set as 4×10^{-4} s, which corresponds to a root-mean-square Courant number of value lower than 2, guaranteeing an accurate resolution of the transient details. Due to the fact that the rotational speed and the flow rate are unsteady at startup process, it is necessary to write the CEL program to control the change in rotational speed and flow rate. According to experimental statistics and related references [32], the variation of the rotational speed N of the impeller can be described by Eq. (9). And the study of transient theory at mixed pump startup, which is presented in detail in Sec. 4, suggests that the variation of the flow rate Q can be derived as the Eq. (10), in which the coefficients are listed in Table 4.

Figure 8 shows that the change of N and Q with time t. One can observe that the rotational speed increases linearly from zero to its rated speed (1450 r/min) in 2 s (marked as t_s), and after 2 s, the speed of the impeller was constant. Besides, the flow rate lags behind the rotational speed to rise to final stable value [11]. Therefore, in our simulation, the time duration of startup process is set to 2 s, and the total calculation time of simulation is set to 4 s. In addition, the inlet boundary condition was set to a total pressure (50 kPa) condition in alignment with the measured data in the experiment, and the outlet boundary condition was set to mass flow rate Q calculated with Eq. (10)

$$N = \begin{cases} 725t, & t \le 2\text{s} \\ 1450, & t > 2\text{s} \end{cases} \tag{9}$$

Table 5 Model parameter data

Parameter	K_ω	K_Q	$\frac{L}{A}$	$\frac{\partial \omega}{\partial t}$	$\frac{1}{g}\frac{L_{pipe}}{S_{pipe}}$	K
Equation	$\int_{R_1}^{R_2} \frac{rdr}{\tan\beta(r)}$	$\frac{1}{2\pi}\int_{R_1}^{R_2} \frac{dr}{rb(r)\sin^2\beta(r)}$	$\frac{L_{Vane}}{A_{Vane}} + \frac{L_{Ribs}}{A_{Ribs}}$	$\frac{\partial \omega}{\partial t}$	$\frac{1}{g}\frac{L_{pipe}}{S_{pipe}}$	$\frac{H_{max}}{Q_{max}}$
Value	0.0026	2.55	3.84	75.92	38.4	197.51

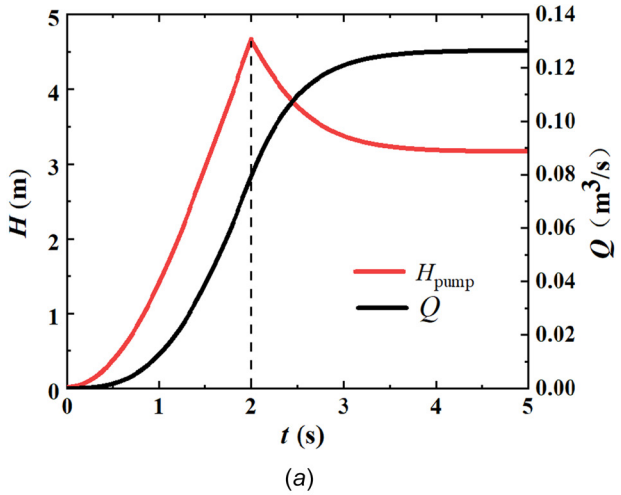

(a)

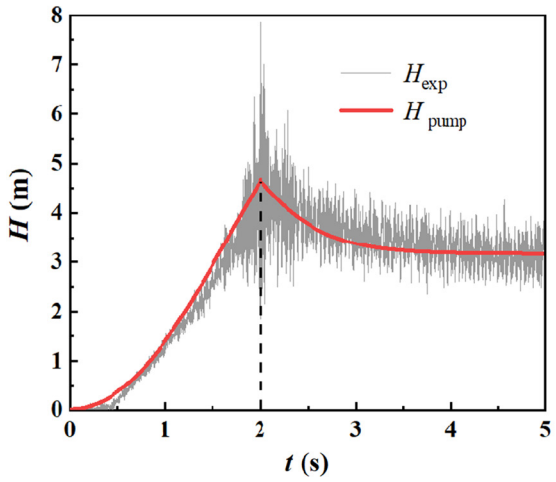

(b)

Fig. 10 Theoretical results and experimental verification ($Z_i = 3$, the startup time $t_s = 2$ s, rated flow rate = 0.126 m³/s, rated head = 2.99 m): (*a*) the flow rate and total head obtained through theoretical solution during the mixed-flow pump startup process and (*b*) comparison of total head H_{pump} obtained by experimental results and analytical solution)

$$Q = a_1 \times \exp(-((t-b_1)/c_1)^2) + a_2 \times \exp(-((t-b_2)/c_2)^2) + a_3 \times \exp(-((t-b_3)/c_3)^2) + a_4 \times \exp(-((t-b_4)/c_4)^2) + a_5 \times \exp(-((t-b_5)/c_5)^2) + a_6 \times \exp(-((t-b_6)/c_6)^2) \quad (10)$$

4 Transient Theory at the Mixed Flow Pump Startup

To maintain the consistency with the mixed-flow pump startup experiment, in which the flow rate in the outlet is changing in time at startup, it is necessary to obtain this change of flow rate for setting the outlet boundary condition in CFD calculation. Dazin et al. [11,12] proposed a theoretical analysis of the fast transients of centrifugal pump and obtained the equation of the transient head. This method is used in this study, and verified by experiment. The detailed derivation is as follows:

Dazin et al. [12] obtained a theoretical expression of the transient total head H_{pump} shown as Eq. (11) by solving the angular momentum equation and energy equation of incompressible fluid. Moreover, the transient total head of the external pipeline also obtained with Eq. (12)

$$H_{pump} = H_s + \frac{1}{g}\left(K_\omega \frac{\partial \omega}{\partial t} - K_Q \frac{\partial Q_v}{\partial t} - \frac{L}{A}\frac{\partial Q_v}{\partial t}\right) \quad (11)$$

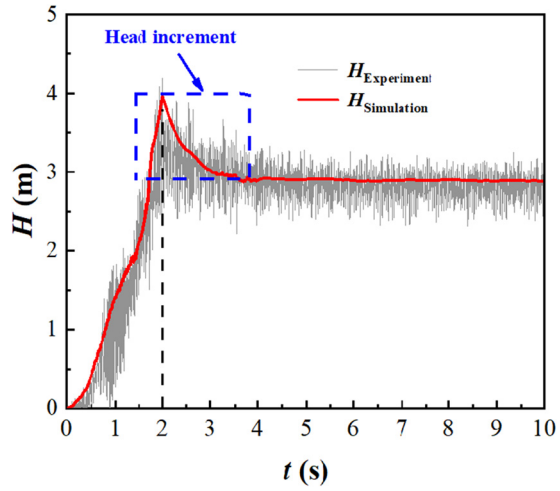

Fig. 11 Comparison of head obtained by experimental and numerical results ($Z_i = 3$, startup time $t_s = 2$ s)

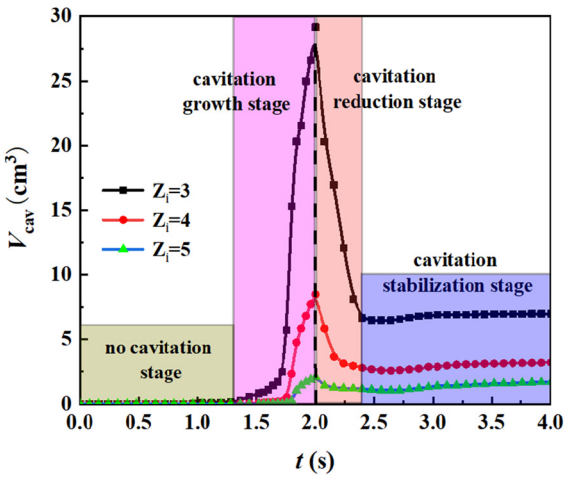

Fig. 12 The simulation results of total volume of cavitation in the impeller with different blade numbers (startup time $t_s = 2$ s, $\sigma = 0.35$)

$$H_{pump} = KQ_V^2 + \frac{1}{g}\frac{L_{pipe}}{S_{pipe}}\frac{\partial Q_v}{\partial t} \quad (12)$$

where KQ_V^2 and H_s are the steady terms; if the pump operates at steady-state, the total head is $H_{pump} = H_s = KQ_V^2$; $\frac{1}{g}\frac{L_{pipe}}{S_{pipe}}\frac{\partial Q_v}{\partial t}$ and $\frac{1}{g}\left(K_Q\frac{\partial Q_v}{\partial t} + \frac{L}{A}\frac{\partial Q_v}{\partial t}\right)$ are the inertial terms; $\frac{K_\omega}{g}\frac{\partial \omega}{\partial t}$ is the angular acceleration term. And the parameters in Eqs. (11) and (12) for this study are shown in Table 5.

As the mixed flow pump is running in a steady-state with a speed of 1450 r/min, the external characteristic curve measured in the experiment is shown in Fig. 9. H_{max} can be obtained using the quadratic function fitting, as shown in Eq. (13)

$$H_{max} = -145.48Q_v^2 - 2.72Q_v + 5.84 \quad (13)$$

where H_{max} is the head when pump is running in a steady-state with a speed of 1450 r/min and Q_v is the volume flow rate.

When the pump is running in a quasi-steady-state, it follows the pump similarity law [1], as shown in Eq. (14):

$$\frac{H_M}{H} = \left(\frac{n_M}{n}\right)^2\left(\frac{D_{2M}}{D_2}\right)^2, \quad \frac{Q_M}{Q} = \left(\frac{n_M}{n}\right)\left(\frac{D_{2M}}{D_2}\right)^3 \quad (14)$$

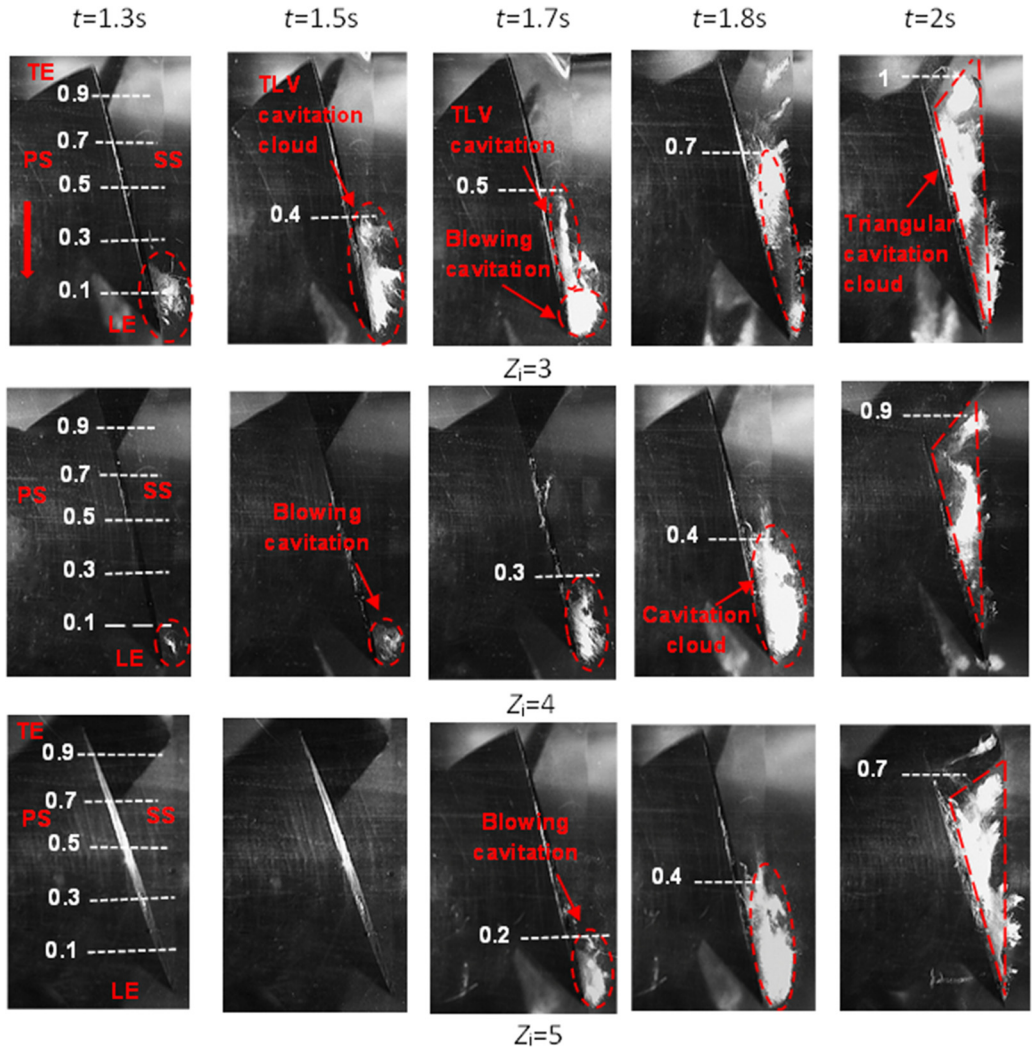

Fig. 13 Comparison of the snapshot images of cavitation in the tip region for the impeller with different blade numbers at startup (startup time $t_s = 2$ s, $\sigma = 0.35$)

Therefore, the quasi-steady head at any rotational speed can be obtained according to the pump similarity law, as shown in Eq. (15)

$$H_s = -145.48Q_v^2 - 2.72\left(\frac{n}{n_{max}}\right)Q_v + 5.84\left(\frac{n}{n_{max}}\right)^2 \quad (15)$$

where H_s is the quasi-steady head at any rotational speed n and n_{max} is equal to the rated rotational speed (n_{max}=1450 r/min).

Then, combining Eqs. (11), (12), and (15), the following equation can be obtained:

$$\frac{\partial Q_v}{\partial t} = \frac{-342.99Q_v^2 - 2.72\left(\frac{n}{1450}\right)Q_v + 5.84\left(\frac{n}{1450}\right)^2 + 0.02}{39.05} \quad (16)$$

Solving the differential Eqs. (16) with MATLAB, and the curve of Q-t can be obtained, and the H_{pump}-t curve can also be obtained by substituting the Eq. (16) into the Eq. (12), these two curves are shown in Fig. 10(*a*). Figure 10(*b*) shows that the H_{pump}-t curve agrees well with the experimental results, which indicates that the transient theory of centrifugal pump [12] can also be applicable to the startup process of mixed flow pumps. Finally, the Eq. (10) can be obtained by Gaussian fitting and embedded into CFD as the outlet boundary condition.

5 Results and Discussion

5.1 Validation of the Numerical Model. In order to validate the numerical results at startup, the performance curve of H-t for

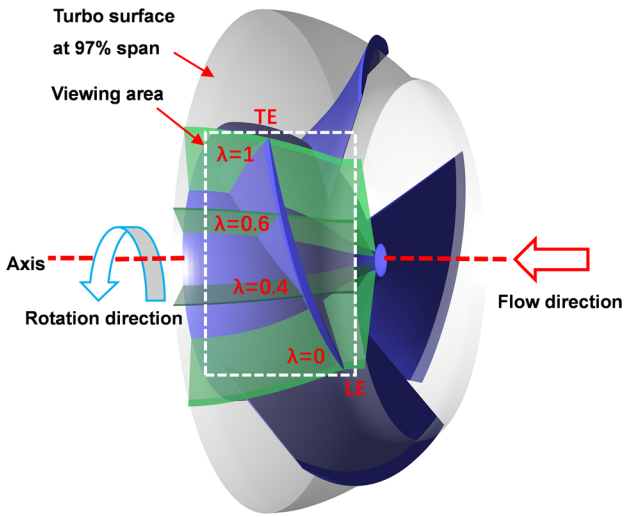

Fig. 14 Schematic diagram of the impeller and the viewing area

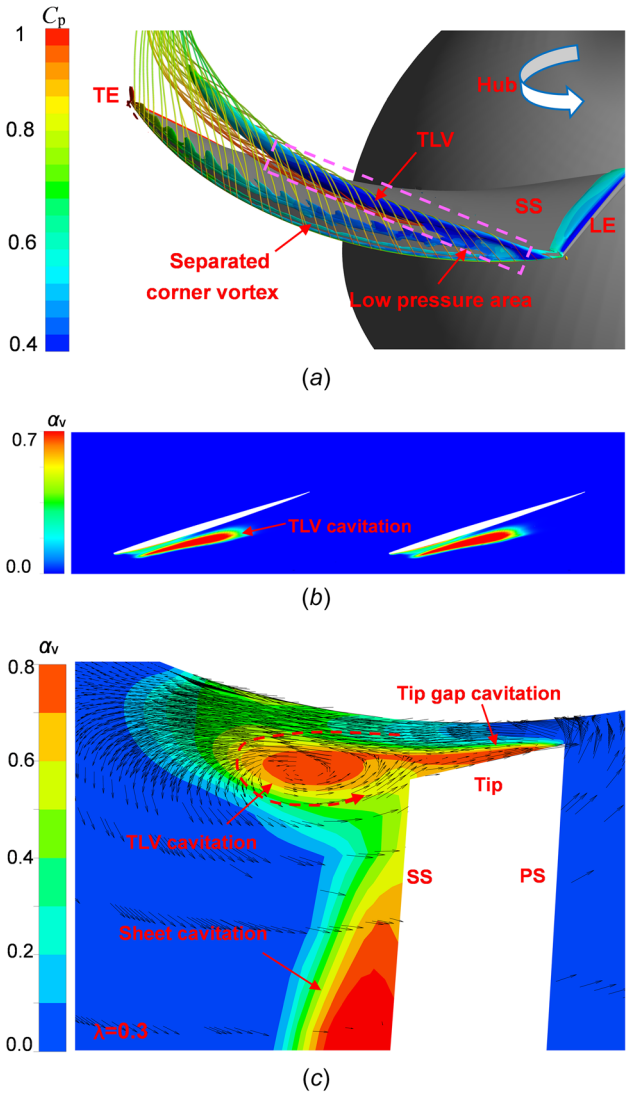

Fig. 15 Tip leakage vortex and tip cavitation of the impeller with $Z_i = 3$ (Startup time $t_s = 2$ s, $\sigma = 0.35$): (*a*) Transient TLV pattern and trajectory at $t = 1.8$ s; (*b*) cavity patterns on turbosurface at 97% span at $t = 1.8$ s (α_v is vapor volume fraction), and (*c*) vapor fraction distribution with velocity vectors at $t = 1.8$ s ($\lambda = 0.3$))

the impeller with blade number $Z_i = 3$ is compared with the experimental results as illustrated in Fig. 11. It indicates that the pump head obtained by the numerical results matches well with the experimental data. The relative errors between the numerical and experimental results are below 3%. Accordingly, it is demonstrated that the numerical model used in this work can be applied to carry out numerical investigation.

The Fig. 11 shows that the transient head produced a head increment during the startup process of the mixed flow pump. The head increment is the difference between the peak head and the final head. The main reason for this peak head is that the rotational speed has reached the final speed at the moment of $t = 2$ s, while the flow rate is only 79.62 L/s ($Q_{(a)} = 79.62$ L/s < 126.62 L/s), as shown in Fig. 8. After 2 s, the rotational speed remains constant at 1450 r/min, but the flow rate continues to increase, which results in a decrease in head. This is the direct cause of the impact value.

5.2 Evolution of Cavitating Volume at Startup. Figure 12 shows the simulation results of total vapor volume in the impeller with different blade numbers during startup ($t_s = 2$ s, $\sigma = 0.35$). The vapor volume V_{cav} is defined as

$$V_{cav} = \sum_{i=1}^{n} \varphi_i V_i \tag{17}$$

where n is the grid number; φ_i is the volume fraction of each grid gas; V_i is the volume of each cell.

The cavitation number σ is defined as

$$\sigma = \frac{P_{in} - P_{va}}{\frac{1}{2}\rho U_{tip}^2} \tag{18}$$

where P_{in} is the inlet pressure, P_{va} is the saturated vapor pressure at ambient temperature, U_{tip} is the tip velocity of the impeller.

The results in Fig. 12 show that during the startup process ($t \le 2$ s), the transient cavitation of the mixed flow pump could be divided into the no cavitation stage and the cavitation growth stage. After the startup process ($t > 2$ s), the transient cavitation could be divided into the cavitation reduction stage and the cavitation stabilization stage. One can observe that, when the rotational speed reaches the rated rotational speed, the vapor volume in the impeller reaches the peak value regardless of blade numbers. However, with the increase of blade number Z_i, the peak value of vapor volume decreases significantly in the cavitation growth stage. The vapor volume in the impeller with $Z_i = 4$ reduced by 75% compared with that in the impeller with $Z_i = 3$, and decreased by 91% in the impeller with $Z_i = 5$. After the rotational speed reaches the rated speed, the vapor volume decreases rapidly and eventually tends to be stable. In the cavitation stabilization stage, the vapor volume in the impeller with $Z_i = 4$ reduces by 60% compared with that in the impeller with $Z_i = 3$, and decreases by 73% in the impeller with $Z_i = 5$. It indicates that the cavitation in the

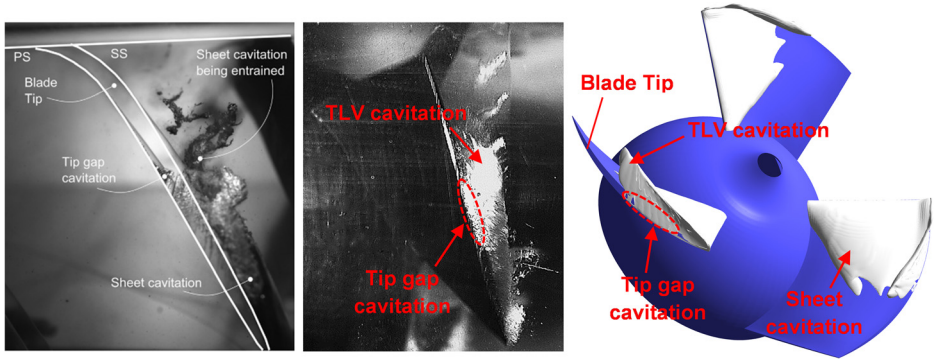

Fig. 16 The tip gap cavitation observed by Tan et al. [22] and the transient experimental and numerical results of the impeller with $Z_i = 3$ at $t = 1.8$ s (startup time $t_s = 2$ s, $\sigma = 0.35$, $\alpha_v = 0.1$). Left: Tan et al. middle: experimental results. Right: numerical results.

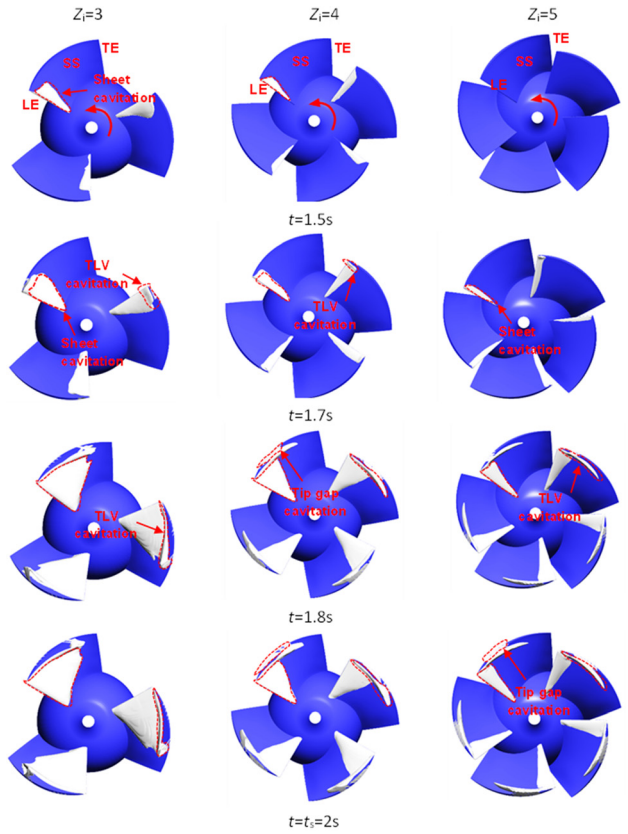

Fig. 17 The variation of the sheet cavitation with the different number of blades at startup (startup time $t_s = 2$ s, $\sigma = 0.35$, $\alpha_v = 0.1$): (*a*) the cavitation growth stage and (*b*) the cavitation reduction stage)

impeller can be effectively suppressed by increasing the number of blades at startup. Sections 5.3 and 5.4 will analyze the effect of the blade numbers on the evolution of different types of cavitation.

5.3 Spatial-Temporal Evolution of Tip Leakage Vortex Cloud Cavitation Patterns at Startup. The transient cavitation occurred in the tip region is extremely complicated during the mixed flow pump startup, including blowing cavitation, TLV

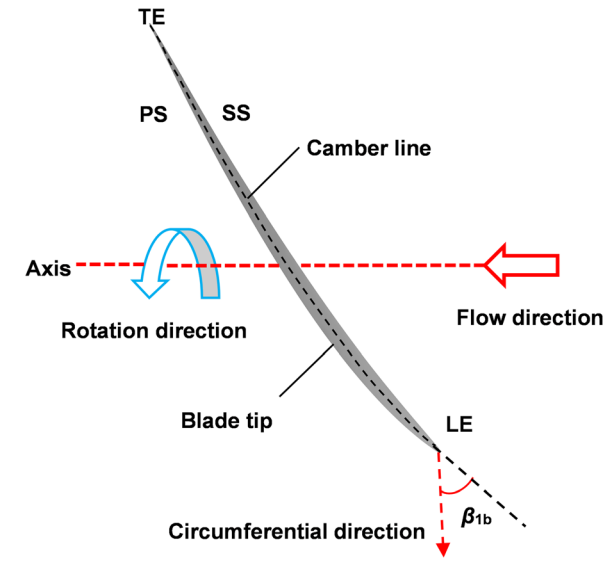

Fig. 18 The schematic diagram of the blade tip (β_{1b} is the blade angle)

cavitation, and tip gap cavitation. Figure 13 illustrates the comparison of the tip cavitation morphology observed at different transient times for the impeller with different blade numbers at $\sigma = 0.35$, $t_s = 2$ s. In this figure, the values shown in the left of white dotted line represent the blade chord ratio, which is defined by $\lambda = s/c$ (where s is the distance from the LE to the section of the blade chord and c is the distance from the LE to the trailing edge) as presented in Fig. 14. The turbosurface at 100% span means the wall of impeller, and the turbosurface at 0% span means the hub of impeller. Thus, the turbosurface at 97% span is between the wall and hub of impeller as shown in Fig. 14.

At instant 1.3 s shown in Fig. 13, the blowing cavitation emerged at the LE of the blade tip. The main reason for the blowing cavitation has depicted in the previous numerical research [23]. The velocity of the jetting flow near the LE was high, which causes the drop of pressure between the pressure surface (PS) and SS. The wall jet emerging from the tip clearance initially maintains the axial momentum and then slows down due to the interaction with the main flow and forms the blowing vortex cavitation near the LE of the blade tip. And this type of cavitation appears differently for the impeller with different blade numbers. The core position of blowing cavitation is about $\lambda = 0.1$ in the impeller

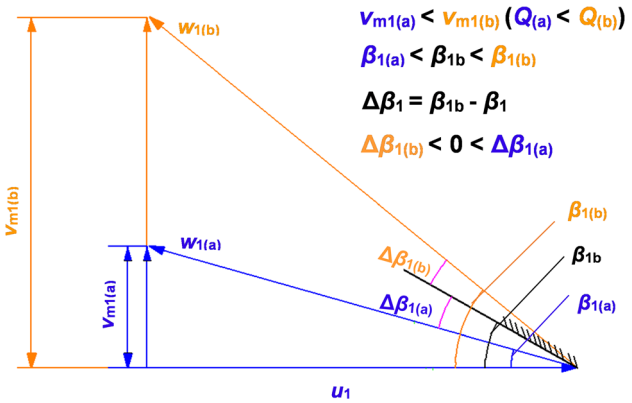

Fig. 19 The schematic diagram of inflow velocity triangle, including two transient flow rate conditions at startup: shown in Fig. 7, (*a*) $Q_{(a)} = 79.62$ L/s, (at $t = 2$ s); (*b*) $Q_{(b)} = 113.16$ L/s, (at $t = 2.6$ s). (u_1 is the circumferential velocity, w_1 is the relative velocity, v_{m1} is the meridional velocity, β_1 is the flow angle, $\Delta\beta_1$ is the incidence angle.)

with $Z_i = 3$, while it is significantly smaller in the impeller with $Z_i = 4$ and 5. For blade number of 4, the blowing cavitation is about located at $\lambda = 0.05$. And for the impeller with $Z_i = 5$, no obvious cavitation is found at instant $t = 1.3$ s until $t = 1.7$ s, and it covers the tip at $\lambda = 0 \sim 0.2$.

At $t = 1.5$ s, the TLV cavitation appears in the impeller with $Z_i = 3$ and converges with the blowing cavitation to form a cavitation cloud which covers the tip area $\lambda = 0 \sim 0.4$. And note that the rotation direction of the TLV is opposite to the direction of the impeller rotation, resulting in the expansion of the TLV cavitation in the chordwise direction. At $t = 1.7$ s, the TLV cavitation in impeller with $Z_i = 3$ covers the tip area $\lambda = 0 \sim 0.5$. For the impeller with $Z_i = 4$, the area of blowing cavitation gradually increases to $\lambda = 0.3$. At $t = 1.7 \sim 1.8$ s, the diameter of the TLV increases gradually from the LE to the trailing edge. The tip leakage cavitating flow along the tip blade chord merges into the TLV in the chordwise direction, resulting in a bit large cavitation clouds at the tip. The cavitation cloud in the impeller with $Z_i = 3$ is elongated and occupies the tip area $\lambda = 0 \sim 0.7$, while the cavitation cloud in the impeller with $Z_i = 4$ and $Z_i = 5$ is stubby and covers the tip area $\lambda = 0 \sim 0.4$. At $t = 2$ s, the rotational speed reaches the rated speed, the cavitation clouds in the three sets of impellers develop into triangular cavitation cloud, which is composed of the blowing cavitation, the tip gap cavitation, and the TLV cavitation. However, the coverage area of triangular cavitation varies at different blade numbers. For $Z_i = 3$, the triangular cavitation cloud covers the whole tip; for $Z_i = 4$, the triangular cavitation cloud is located at $\lambda = 0 \sim 0.9$ of the blade chord; for $Z_i = 5$, the triangular cavitation cloud occupies the chord length coefficient $\lambda = 0 \sim 0.7$.

To clearly analyze the TLV cavitation and the tip-gap cavitation, the transient simulation results for the impeller with $Z_i = 3$ under $t = 1.8$ s, $\sigma = 0.35$, are investigated. For the TLV cavitation, as shown in Fig. 14, the trajectories of TLV is defined by the Q criterion ($1.5 \times 10^6\ s^{-1}$), and the pressure coefficient is defined as $C_p = P/(0.5\rho U_{tip}^2)$. It can be observed that the TLV has a continuous tubular pattern, and it forms near the leading edge of the blade and detaches form the SS. Another point is that the TLV forms a low pressure area, which leads to the formation of the TLV cavitation, as shown in Fig. 15(*c*). Figure 15(*b*) illustrates the cavity patterns on turbosurface at 97% span, and this cavitation morphology matches well with the low pressure area shown in Fig. 15(*a*).

For the tip gap cavitation, as shown in Fig. 16, the simulated cavity was defined as the isosurface of vapor volume fraction of $\alpha_v = 0.1$ in the impeller computational zone. When the leakage flow enters the tip gap, the separated corner vortex occurs at the corner near the PS as shown in Fig. 15(*a*), because the corner with the right angle makes the flow separate near the tip corner [22,23]. The pressure in the separated corner vortex is lower, resulting in the generation of cavitation bubbles in the tip gap. The tip gap cavitation is observed obviously shown in Figs. 15(*c*) and 16, and the numerical results of the cavitating locations show a quite good agreement with the experimental results.

5.4 Spatial-Temporal Evolution of Sheet Cavitation Patters at Startup. It is difficult to clearly capture the cavitation on the SS in the experiment; therefore, the numerical simulation is used to study the evolution of the sheet cavitation. Figure 17 shows the sheet cavitation evolution on the cavitation growth stage and the cavitation reduction stage, through which one can clearly observe the time evolution of sheet cavitation on each impeller, and find the influence of blade number on the sheet cavitation volume.

In the cavitation growth stage, when the pump runs to $t = 1.5$ s, the sheet cavitation appears on the SS of the blade in the impeller with $Z_i = 3$ and $Z_i = 4$, while appears at $t = 1.7$ s for the impeller with $Z_i = 5$. With the rotation speed increasing, the sheet cavitation widens in the tip region, and the chordwise length of sheet cavitation expands in the radial direction. At $t = t_s = 2$ s, the rotational speed reaches the rated speed, and the coverage area of the

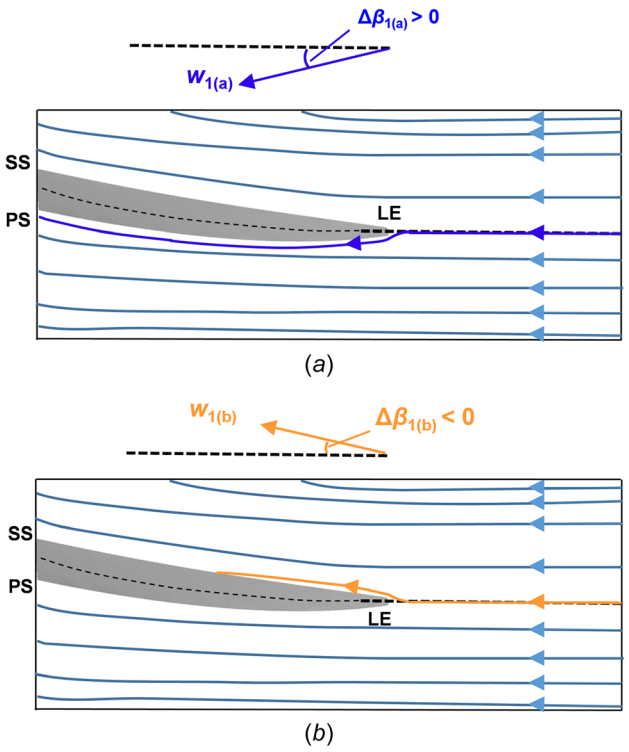

Fig. 20 The streamlines near the LE of blade tip, including two transient flow rate conditions at startup: shown in Fig. 7, (*a*) $Q_{(a)} = 79.62$ L/s (at $t = 2$ s) and (*b*) $Q_{(b)} = 113.16$ L/s (at $t = 2.6$ s)

sheet cavitation reaches peak. The shape of sheet cavitation is triangular. The shape of thin sheet cavity distribution is associated with the incidence angle of the blade and the velocity gradient on the SS of blade. It can be found that the sheet cavitation in the impeller with $Z_i = 3$ is the most serious, occupying almost the entire suction surface, while the cavitation only covers a small part of blade surface in the impeller with $Z_i = 4$, and even only appears in the leading edge in the impeller with $Z_i = 5$. In the cavitation reduction stage, the rotation speed of the impeller keeps constant, and the flow rate reaches the rated value. The coverage area of sheet cavitation all decreases gradually, as shown in instant $t = 2.6$ s, the sheet cavitation has disappeared in the impeller with $Z_i = 5$.

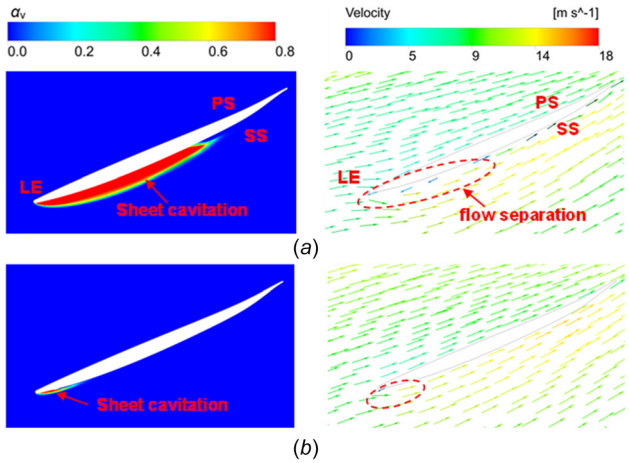

Fig. 21 Stretch-out view of vapor volume distribution (left) and velocity field (right) on turbosurface at 60% span ($Z_i = 3$), including two moments: (*a*) $t = 2$ s and (*b*) $t = 2.6$ s

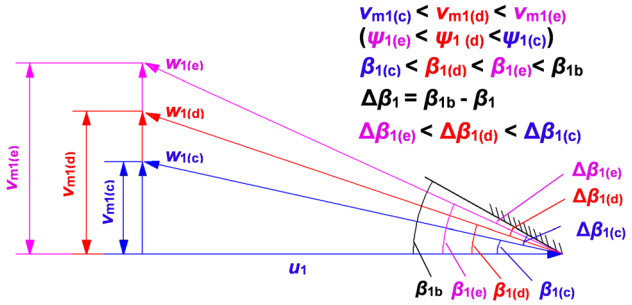

Fig. 22 The schematic diagram of inflow velocity triangle in the impeller with different blade number Z_i at $t = 2$ s ($Q = 79.62$ L/s): (*c*) $Z_i = 3$; (*d*) $Z_i = 4$; (*e*) $Z_i = 5$ (The excretion coefficient is defined as $\psi_1 = 1-(Zs_u/\pi D_1)$; Z is the blade number; s_u is the thickness of blade)

To further study the causes of the formation and disappearance of the sheet cavitation, the transient inflow field in the impeller with $Z_i = 3$ at two instants $t = 2$ s and $t = 2.6$ s are selected to analyze. As shown in Fig. 7, $Q_{(a)} = 79.62$ L/s, $N = 1450$ r/min at t = 2 s; $Q_{(b)} = 113.16$ L/s, $N = 1450$ r/min at $t = 2.6$ s. Figure 18 shows the schematic diagram of the blade tip, β_{1b} is the blade angle. According to the classic design theory of pump, the inlet flow to the LE of blade is mostly axial, so the circumferential component of the absolute inflow velocity (v_u) approximately equals to zero [1]. Based on this assumption, the velocity triangles of the two different flow rates are plotted in Fig. 19. The meridional velocity of inlet is defined as $v_{m1} = Q/(\psi_1 A_1)$, (ψ_1 is the excretion coefficient; A_1 is the area of the inlet section). Therefore, in impeller with $Z_i = 3$, the size of the flow rate ($Q_{(a)}$, $Q_{(b)}$) is corresponding to the size of the meridional velocity ($v_{m1(a)}$, $v_{m1(2)}$). The size of the flow angles ($\beta_{1(a)}$, $\beta_{1(b)}$) is corresponding to the size of the v_m ($v_{m1(a)}$, $v_{m1(2)}$). The incidence angle is defined as $\Delta\beta_1 = \beta_{1b} - \beta_1$, ($\beta_1$ is the flow angle). Figure 20 shows the streamlines near the LE of blade tip at two different flow rates. At $t = 2$ s, the incidence angle $\Delta\beta_{1(a)}$ is a positive value (shown in Fig. 19(*a*)). The positive incidence angle aggravates the flow separation in the SS near the LE of the blade, which decreases the local pressure and promotes the formation of cavitation in the SS, as shown in Fig. 21(*a*). At t = 2.6 s, the incidence angle $\Delta\beta_{1(b)}$ is a negative value (shown in Fig. 19(*b*)). The fluid is transported into the LE of the blade at the negative incidence angle, resulting in the fact that weaken flow separation in the SS near the LE of the blade. It caused that the low pressure recovers and the sheet cavitation on the SS reduces, as shown in Fig. 21(*b*). However, the negative incidence angle decreases the local pressure on the PS and leads to the formation of cavitation on the PS as shown in Fig. 17 (at $t = 2.6$ s, $Z_i = 5$).

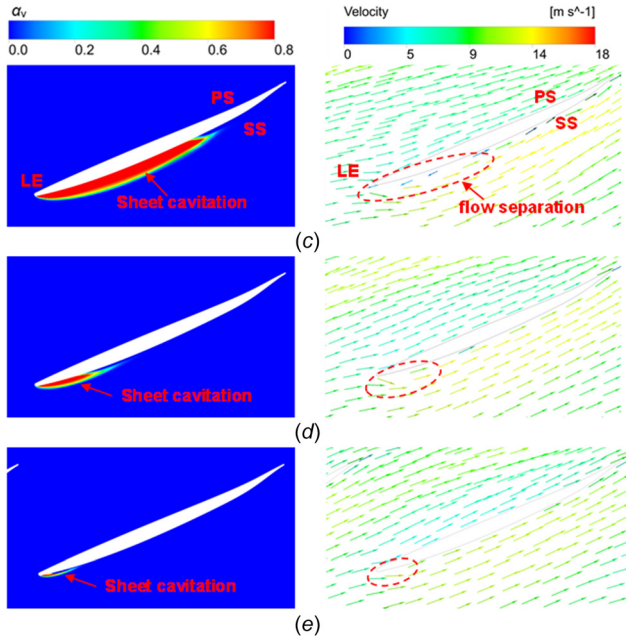

Fig. 23 Stretch-out view of vapor volume distribution (Left) and velocity field (Right) on turbosurface at 60% span ($t = 2$ s), including three blade number: (*c*) $Z_i = 3$; (*d*) $Z_i = 4$; (*e*) $Z_i = 5$

Figure 22 shows the schematic diagram of inflow velocity triangle for the impellers with different blade numbers at $t = 2$ s, ($Q = 79.62$ L/s). The results show that the incidence angle decreases in the same flow rate condition with the blade number increasing, which weaken flow separation in the SS near the LE of the blade, as shown in Fig. 23. This is the reason why at $t = 2$ s the area of sheet cavitation on the SS in the impeller with $Z_i = 5$ is significantly smaller than that with $Z_i = 3$. Moreover, the incidence angle of impeller with $Z_i = 5$ reaches negative value more quickly during startup. Therefore, at the cavitation reduction stage, the sheet cavitation on the SS dissipates faster and the sheet cavitation on the PS forms faster in impeller with $Z_i = 5$, as shown in Fig. 17(*b*).

6 Conclusions

In this paper, the cavitation evolution at startup in the mixed flow pump with different blade numbers was investigated by experimental and numerical methods. The primary conclusions can be summarized as follows:

A numerical methodology for calculating the transient cavitating of mixed flow pump during the startup period was proposed. The predicted results, including the head and transient cavitation, agree well with the experimental results. It reflects that the improved SST k–ω turbulence model, the Zwart cavitation model, and the numerical methodology are capable to analyze the transient cavitation at startup.

The transient cavitation of the mixed flow pump could be divided into four stages: no cavitation stage, the cavitation growth stage, the cavitation reduction stage, and the cavitation stabilization stage. As the number of blades increasing, the total vapor volume decreases about 75% and 60% for impeller with $Z_i = 4$, and decreases about 91%, 73% for impeller with $Z_i = 5$ in the cavitation growth stage and the cavitation stabilization stage, respectively.

As the blade number increasing, the cavitation structures in the tip region present different emerging time, scales and locations in the experimental results. In $Z_i = 3$, the blowing cavitation occurred at $t = 1.5$ s, the triangular cavitation cloud covers almost the whole tip. In $Z_i = 4$ and $Z_i = 5$, the blowing cavitation delayed slightly, and the triangular cavitation cloud covers the range of $\lambda = 0 \sim 0.9$ and $\lambda = 0 \sim 0.7$, respectively.

The spatial-temporal evolution of sheet cavitation at startup is highly related to the blade number and incidence angle. At the cavitation growth stage, the incidence angle is always a positive value and increases with the increase of rotational speed, which enhanced flow separation in the SS near the LE of the blade. At the cavitation reduction stage, the positive incidence angle decrease with the increase of flow rate, which weaken flow separation in the SS near the LE of the blade. The incidence angle decreases in the same flow rate condition with the blade number increasing, which weaken flow separation in the SS near the LE of the blade. The effect of $Z_i = 4$ relative to $Z_i = 3$ on cavitation is more obvious than that of $Z_i = 5$ relative to $Z_i = 4$, and the increase in Z_i promotes the formation of cavitation in the PS. There is no linear relationship between blade numbers Z_i and cavitation suppression effect, so the impeller with $Z_i = 4$ is the best number of blades for this study.

Funding Data

- National Natural Science Foundation of China (Grant No. 51979125; Funder ID: 10.13039/501100001809).

- Key R & D projects in Jiangsu Province (Grant No. BE2021073).
- Jiangsu Outstanding Youth Fund (Grant No. BK20211547).
- Water Conservancy Science and Technology Project in Jiangsu Province (Grant No. 2021007).

Nomenclature

C_p = pressure coefficient
D_0 = impeller inlet diameter, mm
D_1 = inlet pipe diameter, mm
D_2 = discharge pipe diameter, mm
g = gravitational acceleration, m/s^2
H = delivery head, m
N = rotating speed, r/min
n_s = specific speed
P_{in} = the inlet pressure, Pa
P_{va} = saturated vapor pressure, Pa
Q_{opt} = design flow rate, L/s
t_s = startup time
u_1 = circumferential velocity, m/s
U_{tip} = tip velocity of the impeller, m/s
v_{m1} = meridional velocity, m/s
V_{cav} = volume of cavitation, cm^3
w_1 = relative velocity, m/s
Z_i = number of impeller blades
Z_s = Number of stay vane blades
α_v = vapor fraction isosurface
β_1 = flow angle
β_{1b} = blade angle
$\Delta\beta_1$ = incidence angle
λ = blade chord ratio
ρ = density of water, kg/m^3
σ = cavitation number
Φ = flow rate coefficient
Ψ = head coefficient
ψ_1 = excretion coefficient
Ω = rotor angular velocity, rad/s

References

[1] Guan, X., 2011, *Modern Pumps Theory and Design*, Aerospace Press, Beijing, China.
[2] Lian, Y., Tian, B., and Wang, S., 2011, "Simulation and Analysis of the Launching Process of Air-Turbine Pump Launch System," Acta Armamentarii, **32**(2), pp. 155–162.
[3] Wittekind, D., and Schuster, M., 2016, "Propeller Cavitation Noise and Background Noise in the Sea," Ocean Eng., **120**, pp. 116–121.
[4] Korkut, E., and Atlar, M., 2012, "An Experimental Investigation of the Effect of Foul Release Coating Application on Performance, Noise and Cavitation Characteristics of Marine Propellers," Ocean Eng., **41**, pp. 1–12.
[5] Rus, T., Dular, M., Širok, B., Hočevar, M., and Kern, I., 2007, "An Investigation of the Relationship Between Acoustic Emission, Vibration, Noise, and Cavitation Structures on a Kaplan Turbine," ASME J. Fluids Eng., **129**(9), pp. 1112–1122.
[6] Wei, Y., Zhu, L., Zhang, W., and Wang, Z., 2020, "Numerical and Experimental Investigations on the Flow and Noise Characteristics in a Centrifugal Fan With Step Tongue Volutes," Proc. Inst. Mech. Eng., Part C J. Mech. Eng. Sci., **234**(15), pp. 2979–2993.
[7] Tsukamoto, H., and Ohashi, H., 1982, "Transient Characteristics of a Centrifugal Pump During Starting Period," ASME J. Fluids Eng., **104**(1), pp. 6–14.
[8] Tsukamoto, H., Matsunaga, S., Yoneda, H., and Hata, S., 1986, "Transient Characteristics of a Centrifugal Pump During Stopping Period," ASME J. Fluids Eng., **108**(4), pp. 392–399.
[9] Tsukamoto, H., Yoneda, H., and Sagara, K., 1995, "The Response of a Centrifugal Pump to Fluctuating Rotational Speed," ASME J. Fluids Eng., **117**(3), pp. 479–484.
[10] Saito, S., 1982, "The Transient Characteristics of a Pump During Start Up," JSME Int. J., **25**(201), pp. 372–379.
[11] Dazin, A., Caignaert, G., and Bois, G., 2007, "Transient Behavior of Turbomachineries: Applications to Radial Flow Pump Startups," ASME J. Fluids Eng., **129**(11), pp. 1436–1444.
[12] Dazin, A., Caignaert, G., and Dauphin-Tanguy, G., 2015, "Model Based Analysis of the Time Scales Associated to Pump Start-Ups," Nucl. Eng. Des., **293**, pp. 218–227.
[13] Tanaka, T., and Tsukamoto, H., 1999, "Transient Behavior of a Cavitating Centrifugal Pump at Rapid Change in Operating Condition—Part 1, Transient Phenomena at Opening/Closure of Discharge Valve," Nihon Kikai Gakkai Ronbunshu B Hen/Transactions Jpn. Soc. Mech. Eng. Part B, **63**(616), pp. 3984–3990.
[14] Tanaka, T., and Tsukamoto, H., 1999, "Transient Behavior of a Cavitating Centrifugal Pump at Rapid Change in Operating Conditions—Part 2: Transient Phenomena at Pump Startup/Shutdown," ASME J. Fluids Eng., **121**(4), pp. 850–856.
[15] Tanaka, T., and Tsukamoto, H., 1999, "Transient Behavior of a Cavitating Centrifugal Pump at Rapid Change in Operating Conditions—Part 3: Classifications of Transient Phenomena," Nihon Kikai Gakkai Ronbunshu B Hen/Transactions Jpn. Soc. Mech. Eng. Part B, **63**(616), pp. 3984–3990.
[16] Duplaa, S., Coutier-Delgosha, O., Dazin, A., Roussette, O., Bois, G., and Caignaert, G., 2010, "Experimental Study of a Cavitating Centrifugal Pump During Fast Startups," ASME J. Fluids Eng., **132**(2), pp. 365–368.
[17] Duplaa, S., Coutier-Delgosha, O., Dazin, A., and Bois, G., 2013, "X-Ray Measurements in a Cavitating Centrifugal Pump During Fast Start-Ups," ASME J. Fluids Eng., **135**(4), p. 041204.
[18] Wu, D., Wu, P., Li, Z., and Wang, L., 2010, "The Transient Flow in a Centrifugal Pump During the Discharge Valve Rapid Opening Process," Nucl. Eng. Des., **240**(12), pp. 4061–4068.
[19] Wu, D., Jiao, L., and Wang, L., 2008, "Experimental Study on Cavitation Performance of a Centrifugal Pump During Starting Period," J. Eng. Thermophys., **10**, pp. 64–66.
[20] Furukawa, M., Inoue, M., Saiki, K., and Yamada, K., 1999, "The Role of Tip Leakage Vortex Breakdown in Compressor Rotor Aerodynamics," ASME J. Turbomach, **121**(3), pp. 469–480.
[21] Horiguchi, H., Semenov, Y., Nakano, M., and Tsujimoto, Y., 2006, "Linear Stability Analysis of the Effects of Camber and Blade Thickness on Cavitation Instabilities in Inducers," ASME J. Fluids Eng., **128**(3), pp. 430–438.
[22] Tan, D., Li, Y., Wilkes, I., Vagnoni, E., Miorini, R., and Katz, J., 2015, "Experimental Investigation of the Role of Large Scale Cavitating Vortical Structures in Performance Breakdown of an Axial Waterjet Pump," ASME J. Fluids Eng., **137**(11), p. 111301.
[23] Zhang, D., Shi, W., Pan, D., and Dubuisson, M., 2015, "Numerical and Experimental Investigation of Tip Leakage Vortex Cavitation Patterns and Mechanisms in an Axial Flow Pump," ASME J. Fluids Eng., **137**(12).
[24] Zhang, D., Shi, L., Shi, W., Zhao, R., Wang, H., and van Esch, B. P. M., 2015, "Numerical Analysis of Unsteady Tip Leakage Vortex Cavitation Cloud and Unstable Suction-Side-Perpendicular Cavitating Vortices in an Axial Flow Pump," Int. J. Multiphase Flow, **77**, pp. 244–259.
[25] Miorini, R., Wu, H., Tan, D., and Katz, J., 2011, "Three-Dimensional Structure and Turbulence Within the Tip Leakage Vortex of an Axial Waterjet Pump," Asme-Jsme-Ksme Joint Fluids Engineering Conference, Hamamatsu, Japan, July 24–29, pp. 271–281.
[26] Wu, H., Miorini, R., and Katz, J., 2011, "Measurements of the Tip Leakage Vortex Structures and Turbulence in the Meridional Plane of an Axial Water-Jet Pump," Exp. Fluids, **50**(4), pp. 989–1003.
[27] Miorini, R., Wu, H., and Katz, J., 2012, "The Internal Structure of the Tip Leakage Vortex Within the Rotor of an Axial Waterjet Pump," ASME J. Turbomach., **134**(3), p. 031018.
[28] Zhao, X., Liu, T., Huang, B., and Wang, G., 2020, "Combined Experimental and Numerical Analysis of Cavitating Flow Characteristics in an Axial Flow Waterjet Pump," Ocean Eng., **209**, p. 107450.
[29] Wang, L., Li, Z., and Dai, W., 2008, "2-D Numerical Simulation on Transient Flow in Centrifugal Pump During Starting Period," J. Eng. Thermophys., **29**(8), pp. 1319–1322.
[30] Wu, D., Xu, B., and Li, Z., 2009, "Numerical Simulation on Internal Flow of Centrifugal Pump During Transient Operation," J. Eng. Thermophys., **30**(5), pp. 1319–1322.
[31] Li, Z., Wu, D., Wang, L., and Huang, B., 2010, "Numerical Simulation of the Transient Flow in a Centrifugal Pump During Starting Period," ASME J. Fluids Eng., **132**(8), p. 081102.
[32] Li, Z., Wu, P., Wu, D., and Wang, L., 2011, "Experimental and Numerical Study of Transient Flow in a Centrifugal Pump During Startup," J. Mech. Sci. Technol., **25**(3), pp. 749–757.
[33] Zhang, Y., Li, Y., Zhu, Z., and Cui, B., 2014, "Computational Analysis of Centrifugal Pump Delivering Solid–Liquid Two-Phase Flow During Startup Period," Chin. J. Mech. Eng., **27**(1), pp. 178–185.
[34] ASME, 2005, *Test Uncertainty*, The American Society of Mechanical Engineers, New York, Standard No. PTC 19.1.
[35] Coleman, H. W., and Steele, W. G., 1989, *Experimentation and Uncertainty Analysis for Engineers*, Wiley, New York.
[36] Shen, X., Zhang, D., and Xu, B., 2020, "Experimental Investigation of the Transient Patterns and Pressure Evolution of Tip Leakage Vortex and Induced-Vortices Cavitation in an Axial Flow Pump," ASME J. Fluids Eng., **142**(10), p. 101206.
[37] Zwart, P., Gerber, A., and Belamri, T., 2004, "A Two-Phase Flow Model for Predicting Cavitation Dynamics," Fifth International Conference on Multiphase Flow, Yokohama, Japan, No. 152.
[38] Menter, F. R., 2009, "Review of the Shear-Stress Transport Turbulence Model Experience From an Industrial Perspective," Int. J. Comput. Fluid Dyn., **23**(4), pp. 305–316.
[39] Bardina, J. E., Huang, P. G., and Coakley, T. J., 1997, "Turbulence Modeling Validation, Testing, and Development," NASA, Washington, DC, Technical Report Memorandum No. 110446.

[40] Reboud, J. L., Stutz, B., and Coutier, O., 1998, "Two-Phase Flow Structure of Cavitation: Experiment and Modelling of Unsteady Effects," Third International Symposium on Cavitation, Grenoble, France, No. 26.
[41] Dular, M., Bachert, R., Stoffel, B., and Sirok, B., 2005, "Experimental Evaluation of Numerical Simulation of Cavitating Flow Around Hydrofoil," Eur. J. Mech. B-Fluids, **24**(4), pp. 522–538.
[42] Leroux, J. B., Coutier-Delgosha, O., and Astolfi, J. A., 2005, "A Joint Experimental and Numerical Study of Mechanisms Associated to Instability of Partial Cavitation on Two-Dimensional Hydrofoil," Phys. Fluids, **17**(5), p. 052101.
[43] Coutier-Delgosha, O., Fortes-Patella, R., and Reboud, J. L., 2003, "Evaluation of the Turbulence Model Influence on the Numerical Simulations of Unsteady Cavitation," ASME J. Fluids Eng., **125**(1), pp. 38–45.
[44] Coutier-Delgosha, O., Courtot, Y., Joussellin, F., and Reboud, J. L., 2004, "Numerical Simulation of the Unsteady Cavitation Behavior of an Inducer Blade Cascade," AIAA J., **42**(3), pp. 560–569.
[45] Ji, B., Luo, X., Peng, X., Wu, Y., and Xu, H., 2012, "Numerical Analysis of Cavitation Evolution and Excited Pressure Fluctuation Around a Propeller in Non-Uniform Wake," Int. J. Multiphase Flow, **43**, pp. 13–21.
[46] Li, Z. R., 2012, "Assessment of Cavitation Erosion with a Multiphase Reynolds-Averaged Navier–Stokes Method," Ph.D. thesis, Delft University of Technology, Delft, The Netherlands.
[47] Liu, J. T., Liu, S. H., Wu, Y. L., Jiao, L., Wang, L. Q., and Sun, Y. K., 2012, "Numerical Investigation of the Hump Characteristic of a Pump-Turbine Based on an Improved Cavitation Model," Comput. Fluids, **68**, pp. 105–111.